VIP

Fine Structures of Zeolite-Linde-L (LTL): Surface Structures, Growth Unit and Defects

Tetsu Ohsuna,[a, b] Ben Slater,*[c] Feifei Gao,[d] Jihong Yu,[d] Yasahiro Sakamoto,[b, e] Gaugshan Zhu,[d] Osamu Terasaki,*[b, e] David E. W. Vaughan,[f] Shilun Qiu,[d] and C. Richard A. Catlow[c, g]

Abstract: High-resolution electron microscopy (HREM) has been used to image the surface structure of nano- and micrometer-sized synthetic crystals of zeolite-Linde-L (LTL). Columnar holes and rotational, nano-sized, wheel-like defects were observed within the crystals, where the hole has a minimum size equal to that of the rotational defect. Predictions of surface structure from atomistic computer simulation concur with the observations from HREM and provide insight into the crystal growth mechanism of perfect and defective LTL. Analysis of the energetics of the formation of rotational defect structures reveals that the driving force for defect creation is thermodynamic and furthermore, the rotational defects could be created in high concentrations. Formation of a columnar hole is found to be slightly energetically unfavourable and therefore we speculate that the incidence of both rotational and nano-sized vacancy defects is strongly dependent on kinetic factors and reaction conditions. The morphology of nano- and microcrystalline LTL is contradistinct and we use insights from simulation to propose an explanation of the disparity in crystal shape.

Keywords: computer simulations · defects · electron microscopy · surfaces · zeolites

Introduction

Linde-L (LTL) was first synthesized by Breck and Flanigen[1] and noted to be a "large-pore" zeolite as was confirmed by the structure analysis of Barrer and Marshall[2] showing it to have 12-ring channels, and the natural mineral perlialite was later shown to be isostructural with LTL.[3] Major interest in LTL was stimulated in 1980 when Bernard[4,5] reported that Pt-K-LTL was a highly selective catalyst for the aromatisation of hexane to benzene. A decade of intensive research and development followed, resulting in a commercial process in the early 1990s.[6,7] More recently LTL has attracted interest as a tubular "nano-container" for metals[8] and photochemically reactive organic molecules.[9]

Zeolite LTL has a one-dimensional (1D) channel with 12-ring undulating channels. The structure was solved by powder X-ray diffraction (XRD) and shown to occupy space group *P6/mmm* with $a = 1.84$ nm and $c = 0.75$ nm (Figure 1a). The structure contains two important secondary building units of cancrinite (CAN) cage and double hexagonal ring (D6R), alternating to form a column (shown in Figure 1b). The columnar structure can be considered to form from CAN cages fusing, giving a D6R between the CAN cages, or more complex growth mechanisms involving D6R and subunits of a CAN structure. The structure can be described by a two-dimensional hexagonal arrangement of the

[a] Dr. T. Ohsuna
Institute for Materials Research
Tohoku University, Sendai 980–8577 (Japan)

[b] Dr. T. Ohsuna, Dr. Y. Sakamoto, Prof. O. Terasaki
Present address: Structural Chemistry, Arrehenius Laboratory
Stockholm University, 10691 Stockholm (Sweden)
Fax: (+46) 816-3118
E-mail: terasaki@struc.su.se

[c] Dr. B. Slater, Prof. C. R. A. Catlow
Davy Faraday Research Laboratory
The Royal Institution of Great Britain
21 Albemarle Street, London, W1S 4BS (UK)
Fax: (+44) 207-629-3569
E-mail: ben@ri.ac.uk

[d] Dr. F. Gao, Prof. J. Yu, Prof. G. Zhu, Prof. S. Qiu
State Key Laboratory of Inorganic and Preparative Chemistry
Jilin University, Changchun 130023 (P.R. China)

[e] Dr. Y. Sakamoto, Prof. O. Terasaki
Department of Physics, Tohoku University
Sendai 980–8578 (Japan)

[f] Prof. D. E. W. Vaughan
Materials Research Institute
Pennsylvania State University
University Park, PA 16802 (USA)

[g] Prof. C. R. A. Catlow
Christopher Ingold Laboratories
University College London
20 Gordon Street, London WC1H 0AJ (UK)

 DOI: 10.1002/chem.200306064

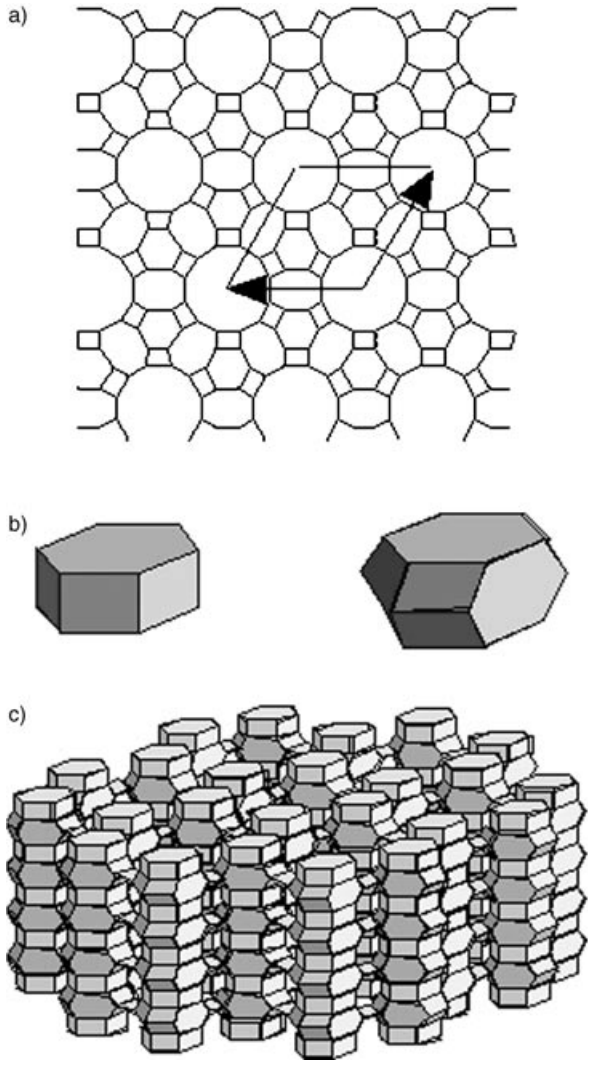

Figure 1. a) Schematic drawings of the framework structure of zeolite LTL, the arrow pointing left indicates the [010] incidence, the arrow pointing north-east indicates the [100] direction. b) Secondary building units of CAN cage and D6R, c) and external crystal surface.

columns ($a = 1.84$ nm) forming 8-ring and 12-ring channels and the crystals generally adopt the form of cylinders or hexagonal prisms, for which the {001} surface is at the top and the bottom of the cylinder, and the sidewalls are {100} and {110} planes (Figure 1c).

A substantial body of synthetic work was performed in the 1980s, supporting the results of the catalysis work, which showed that control of crystal size and shape was necessary for optimisation of catalytic aromatisation properties.[10] LTL is readily made from potassium aluminosilicate gels at temperatures between 90 and 200 °C. Compositionally LTL can be made with Si/Al ratios from 1 to about 3.5, designated as Ba-GL[11] (Si/Al = 1 to 1.5), ECR-2[12] (Si/Al = 1.5 to 2.6) and Linde-L (Si/Al = 2.6 to 3.5). Nanocrystals are formed when large alkylammines are included in the reaction gels;[13] hexagonal columnar crystals up to 5 μm long can be made at higher temperatures;[14] prisms and discs up to 1 μm in diameter are typical in many higher temperature preparations. The morphology of the crystal is controlled by a combination of factors such as gel stoichiometry, seeding, and time and temperature of crystallisation. Metakaolin may be an effective aluminosilicate source for LTL syntheses,[15,16] where smaller kaolin crystals yield smaller crystal LTL products.

To control crystal size, morphology and defect formation it is important to understand the growth mechanism(s) that can often be deduced from analysis of sub-structures (such as secondary building units (SBUs)), crystal defects and surface structures. The first may be observed and engineered through nanocrystal syntheses[17] and the latter by careful examination and computer modelling of crystal edges and surfaces.[18,19] An important feature of LTL crystallisations is that it often co-crystallises with offretite (OFF) and erionite (ERI). Apparent epitaxial interfaces have been observed in "hammer" (OFF shaft-LTL head)[21] and "ring" (OFF "finger"-LTL ring)[18] crystal associations in low magnification microscopy studies. Stacking faults have also been observed in high-resolution images of LTL[22] that has a supermesh structure $R\sqrt{13}\cdot\sqrt{13}$ which entails a rotation of one part of the crystal on the {001} planes through 32.2°; termed a coincidence boundary. Herein, we describe new types of defects that have been located by using advanced HREM imaging methods.[23] We then attempt to rationalise the existence and size of these defects using computer simulation methods. Finally, we discuss how the surface structure and the observation of a disparate range of defects can be used to suggest a crystal growth mechanism based upon assembly of building units and we speculate on how the crystal habit may be affected by the mode of assembly.

Experimental Section

Synthesis of nanocrystalline, K LTL: In this study, LTL nano crystals were made with a gel stoichiometry $1.0\,Al_2O_3{:}30\,SiO_2{:}10\,K_2O{:}400\,H_2O$ by using the recipe employed by Meng et al.,[24] in which KOH (5.82 g; Sigma, pellets, ≥85 %) was initially allowed to react with fumed silica (12 g; Sigma, 99.8 %) in distilled water (36.8 g) to give solution I. A potassium aluminate solution (solution II) made from KOH (2.91 g; Sigma) and $Al(OH)_3$ (1.04 g; Sigma) in distilled water (10 g) was then added to solution I. Each component solution was first cooled then filtered after heating in an autoclave at 443 K, prior to mixing. The resultant mixture was placed in the Teflon-lined stainless steel autoclaves at 443 K for six days. After centrifuging and washing, the sample was dried at 343 K in an oven. Powder X-ray diffraction (XRD) patterns were recorded in step scanning on a Philips PW3050 X-ray diffractometer by using $Cu_{K\alpha}$ radiation ($\lambda = 1.5418$ Å) with a graphite monochromator in the diffracted beam path. The average size of the nanoparticles was 100 nm analysed on the basis of the Debye–Scherrer equation ($D = 0.89\lambda/\beta\cos\theta$, where D is the crystal size, λ the wavelength ($Cu_{K\alpha}$), β the corrected half-width of the (221) diffraction line of LTL, and θ the diffraction angle). Inductively coupled plasma (ICP) analysis performed on a Perkin-Elmer Optima 3300DV spectrometer gave the Si/Al ratio of the as-made LTL nanocrystals as 2.905, and the Al/K ratio as 1.05. Samples were evaluated in the microscopy experiments without further treatment.

Synthesis of micron-sized, K LTL: Micrometre-sized crystals of zeolite L were synthesized by first reacting silica sol (≥28 %) (21.46 g) in H_2O (6.5 g) which was mixed until homogenous (solution I). This mixture was then added to a potassium aluminate solution (solution II) made from KOH (3.22 g) and Al powder (0.54 g) in H_2O (6.54 g). The resultant mixture was placed in the Teflon-lined stainless steel autoclave at 453 K for two days. After washing, the sample was air-dried at 423 K in an oven. The approximate molar ratio for the mixture was $2.35\,K_2O{:}1\,Al_2O_3{:}$

$10SiO_2$:$160H_2O$ and the product ratios were determined to be $SiO_2/Al_2O_3 = 6.23$, $K_2O/Al_2O_3 = 0.964$ and $K_2O/SiO_2 = 0.156$, by ICP.

Standard preparation of micron-sized Na/K LTL: Zeolite L was synthesized by using colloidal silica (≥28%), $Al(OH)_3$ (≥98%), KOH (≥98%) and NaOH(≥98%). $Al(OH)_3$ (0.54 g, Sigma) was dissolved in a solution of KOH (1.68 g), NaOH (1.20 g) and water (6.23 g) at a temperature of 373 K followed by cooling to room temperature. After vigorous stirring, colloidal silica (20.25 g) was added with water (7.38 g) to form a mixture, which was then vigorously stirred for a few minutes, until a thick gel was formed. The resultant gel was placed in the Teflon-lined stainless steel autoclave at 433 K for six days. After cooling, the upper part of the strongly alkaline solution was decanted, whilst the remaining white residue was washed with water until it remained neutral. This product was then air-dried for 12 h at room temperature. The original molar ratio of the reagents was $3.172M_2O$:$1Al_2O_3$:$10SiO_2$:$165.58H_2O$ (50% NaOH,50% KOH). The final composition of the sample was determined to be $SiO_2/Al_2O_3 = 6.83$, $M_2O/Al_2O_3 = 1.00$ and $K_2O/SiO_2 = 0.271$ by ICP.

The three synthesis routes differ in a number of key experimental parameters, such as the Si:Al ratio of the reagents, the identity of the extra-framework species, the duration of synthesis and the ageing time. The microcrystalline crystals have similar average crystal sizes and shapes, though the average size of the crystal where Na is present appears to be slightly larger than in the pure K synthesis. The aspect ratio and crystal shape of the nano- and microcrystals differs dramatically. In the nanocrystal the *c*/*a* ratio is much larger than that in the microcrystals. We will return to the reason for these differences in the Discussion.

Electron microscopy: The samples were investigated with JEM-3010 (operating at 300 kV, Cs = 0.6 mm, structural resolution 1.7 Å) and JEM-4000EX (operating at 400 kV, Cs = 1.0 mm, structural resolution 1.7 Å) electron microscopes. Images and diffraction patterns were recorded with films and a CCD-camera (Model 794, Gatan, size 1024 × 1024, pixel size $25 \times 25\ \mu m^2$) using low dose conditions.[23]

The low-magnification electron microscopy (EM) image of nanocrystal LTL shows clearly that the crystal is cylindrical in shape and is very well crystalline (Figure 2a). In powder or nanocrystals of LTL, the size of the *c* plane is fairly large compared to the length along the *c* axis, and it is difficult to obtain the zone axes other than [001] in the nanocrystals. However, we note that a recently synthesised single crystal of LTL shows the opposite aspect ratio.[25]

SEM images of single crystals of LTL were observed on a JEOL 6700F SEM at 5 kV. The micrometer-sized crystals were coated with Pt/Pd to obtain electrical conductivity on the surface. An example of the micron-sized crystal is shown in Figure 2b. Note the presence of an unusual hole at the top of the cylindrical crystal that appears to extend into the interior of the crystal. The pure K and Na/K micrometer-sized crystals are shown at lower magnification in Figure 2c and 2d.

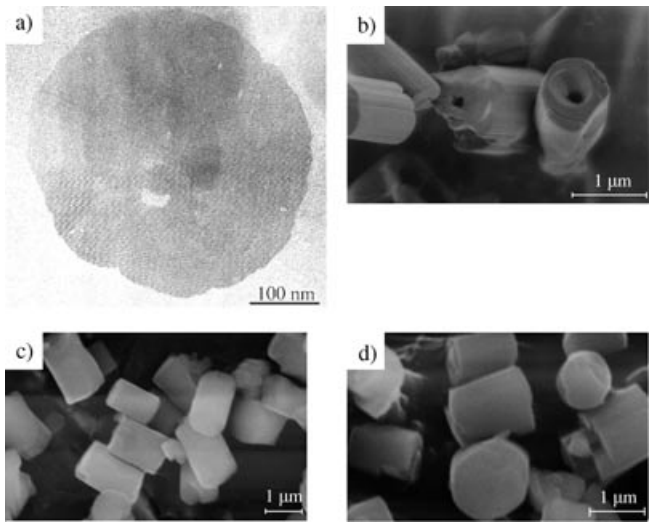

Figure 2. a) TEM image of nano-LTL, b) SEM image of micro-LTL, c) SEM image of K-LTL, and d) SEM image of Na/K-LTL.

Results

In the following sections, we report the analysis of nano-sized crystals of LTL, in which the results are compared with those obtained for microcrystalline samples.

Surface structure: Figure 3a–c show the observed HREM images of an edge on view with [100], [110] and [001] incidences, respectively. Comparison of these images with simulated ones from different surface structure models, allows us to deduce the surface structures of LTL. We find that firstly, the framework is terminated not with CAN cages but with D6R units on the {001} surface, and secondly, that the sidewall of the crystal is terminated with CAN cages, as was shown schematically in Figure 1c. Further details of the assignment of the surface structure have been discussed by Ohsuna et al.[26] The {001} surface is found not to exhibit a D6R free surface. For both nano- and microcrystals, identical surface terminations were

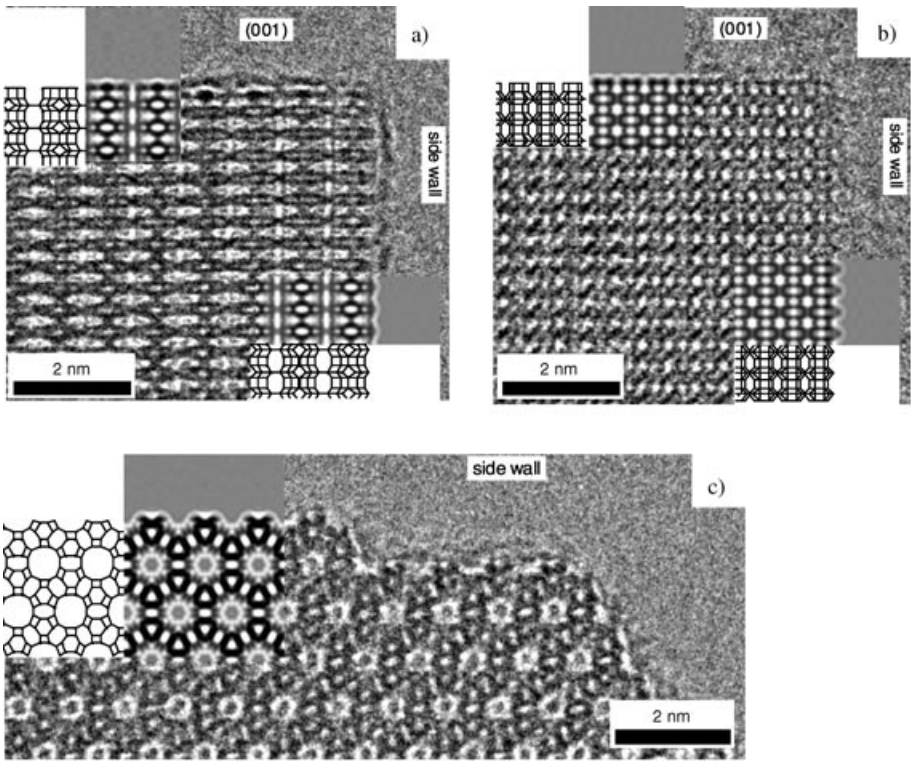

Figure 3. HREM images of LTL surfaces a) [100], b) [110], and c) [001] incidences (taken from reference [22]).

observed for each distinct crystallographic plane. We emphasise this point, since it provides important evidence that the atomic growth mechanism is identical in both nano- and micron-sized crystals and hence it is reasonable to assert that it is chiefly *kinetic* rather than thermodynamic factors that determine the relative growth rate of distinct crystal faces and therefore, the crystal shape.

Rotational defects in the framework: An HREM image taken with the [001] incidence is shown in Figure 4. Looking

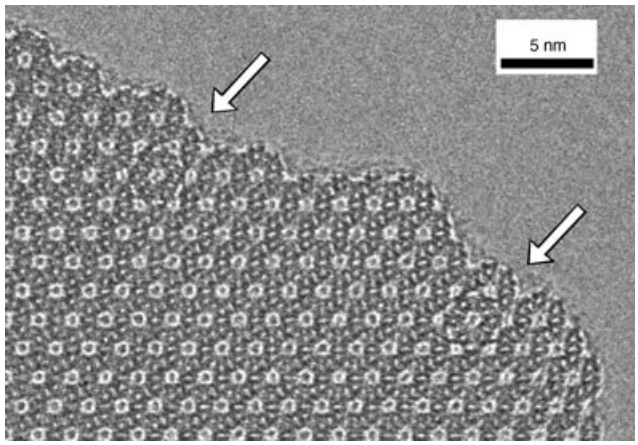

Figure 4. HREM image of rotational defects indicated with arrows, [001] incidence.

at the image from a distance, one can see deformed channels, which are clearly different from the other channels, indicated by arrows within the figure. From this observation, a columnar defect model of the LTL framework was devised that consisted of a group of six "cancrinite" columns surrounding one main 12-ring channel rotated 30° as a unit around the *c* axis (shown schematically in Figure 5). A simulated image based on the model was calculated by the multislice method.[26] The simulated image fitted perfectly over the experimental HREM image and hence we believe the structure of the defect has been identified. The rotation produces six deformed channels and six 8-ring channels which give different contrasts in the HREM image. The central 12-ring channel, which provides access into the crystal interior appears not to be deformed and hence its ability to uptake atoms or molecules is unlikely to be affected by the rotation.

Nanosized columnar defects: A peculiar bright contrast is observed in TEM images taken with [001] incidence. The contrast indicates no framework was formed at the place from the top to the bottom and consequently a straight channel with larger diameter was formed along the *c* axis—a "columnar hole". The structure of the nano-defect imaged by HREM is shown in Figure 6b. Note that the minimum size of this defect corresponds exactly to the size of rotational defect mentioned above. Although the holes can be formed with much greater sizes than the 12-ring surrounded by six CAN/D6R columns, the fact that no smaller defects are observed may be significant. There is no evidence that a single CAN/D6R column can be extracted from the structure. Conversely, there does not appear to be an upper limit to the size of the columnar hole. In Figure 6b, the maximum length is in excess of 100 nm but by comparison with Figure 2b, the size can extend up to much greater length scales.

Static lattice simulation

Surface structure {1$\bar{1}$0} and {110}: In previous work,[19,27] we have described how predictions of zeolite surface structure can be made by using static lattice simulation methods. Details of the general simulation strategy are described in reference [28] and more specifically in references [19,27,29]. To summarise briefly, we use the GULP[30] and MARVIN[28] codes to relax the atomic positions to zero net force within the crystal bulk and surface structure, respectively, and use the interionic potentials derived by Sanders and Catlow[31] to describe the interactions between atoms. The two-region surface repeat unit used for the surface relaxations consisted of an upper layer, relaxed explicitly, containing four complete layers and a lower region held fixed, which also contained four layers. The number of species in the two regions exceeded 1400 for each surface considered.

We begin by examining the faces that are observed in the experimental morphology, and other faces with large interlayer spacing. In this case, we expect the {1$\bar{1}$0} (or {100}), {110} and {001} faces to dominate in the crystal morphology. Cleavage of low-symmetry materials gives rise to a large number of potential terminating surface structures, but in fact, we find that by using the criterion of surface energy, which is inversely proportional to thermodynamic stability, we can readily determine that low index faces have very few low-energy terminating structures. For instance, assessment of the relative stability of various possible terminations of the

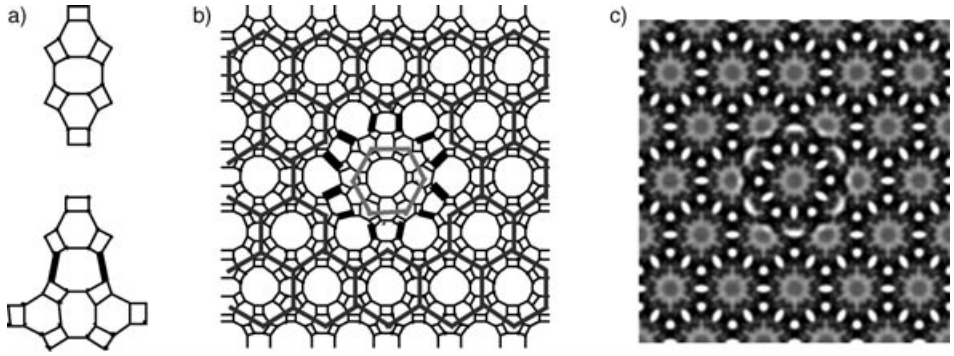

Figure 5. Schematic model for the rotational defects. Connectivity of the column in forming 8-rings for perfect (a), rotational defect(b) and matching of rotational defect to the perfect crystal (c). Simulated image for the rotational defect at specimen thickness of 10 nm, defocus of OL −68 nm.

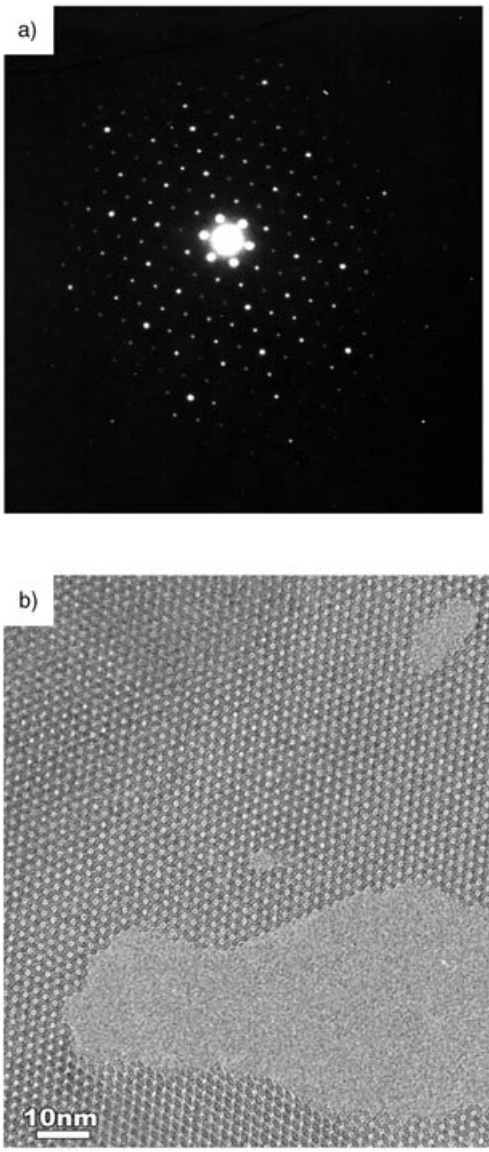

Figure 6. a) ED pattern taken with incidence down the [001] axis, b) TEM image of LTL taken with [001] showing columnar holes with different sizes. The minimum size observed is 1 main 12 MR channel surrounded by six columns containing CAN and D6R building units.

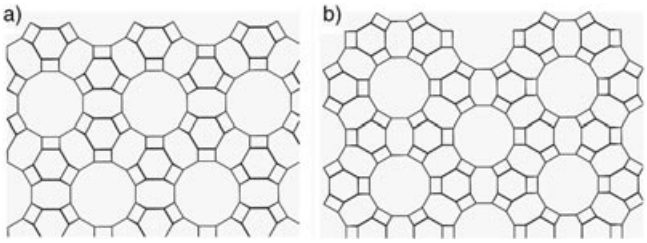

Figure 7. The $\{1\bar{1}0\}$ (a) and {110} surfaces (b) of LTL shown in cross section. Only the silicon atoms are depicted, for clarity. The left-hand figure corresponds to the most stable $\{1\bar{1}0\}$ surface, whilst the right-hand surface is the {110} termination. Both structures can be readily observed by comparison with Figure 3c. The left-hand portion of the Figure 3c is equivalent to Figure 7a, exposing a single terminal CAN cage. The right-hand side of Figure 4 shows the {110} termination and is equivalent to Figure 7b, displaying two terminal CAN cages.

$\{1\bar{1}0\}$ surface, shows that the termination shown in Figure 7a has the lowest unique surface energy (0.71 Jm^{-2}). Additionally, we considered the {110} surface and again determined a single unique termination, similar but not identical to that found for the $\{1\bar{1}0\}$ surface with a slightly higher surface energy of 0.84 Jm^{-2}, shown in Figure 7b, where the silicon atomic positions are found at the vertices within the figure. The upper part of the Figure corresponds to the crystal external surface and is shown in cross section in Figure 7 and differs by the number of CAN cages exposed at the crystal exterior. In Figure 7a, the terminating structure exposes a single CAN cage lying in the same plane (at the surface), in Figure 7b, two CAN cages are exposed that lie in the same plane. The surface energies reflect the relative stability of the surfaces and can be rationalized by considering the number of dangling bonds formed at each face. In the $\{1\bar{1}0\}$ case, two dangling bonds per surface repeat unit are formed upon cleavage, but for the {110} case four bonds are created. Therefore we expect the $\{1\bar{1}0\}$ surface to be most stable on the grounds that the higher the number of terminating bonds exposed, the more thermodynamically unstable the surface is.

By reference to the HRTEM images in Figure 3c and Figure 4, we find that the surface structures predicted to be the most stable from thermodynamic considerations are readily observed. Evidently, the predicted structures correspond exactly with those observed, exhibiting CAN cages at the external surface in a crenellated fashion. The experimental images clearly identify two distinct terminations of $\{1\bar{1}0\}$ and {110} character, with one and two terminal CAN cages lying parallel to the crystal surface in Figure 3c and Figure 4 respectively. The {110} surface with double CAN cages can be seen less prevalently in Figure 3c as step edges, but is more easily distinguished in Figure 4, where the majority of the surface is double CAN cage terminated. On the basis of thermodynamic considerations, we would expect the $\{1\bar{1}0\}$ surface to dominate in the morphology, which is indeed confirmed by inspection of the microcrystalline sample.

Surface structure {001} surface: For the {001} surface, we identified two terminations of equal stability, with surface energies of 2.12 Jm^{-2}, one of which is shown in Figure 8. Two different crystal surface orientations are shown, to facilitate a comparison with the experimental HRTEM images in Figure 3a and 3b. Clearly, the D6R is evident in each case; the left-hand structure of Figure 8 corresponds exactly with Figure 3a, whilst the right-hand structure corresponds to Figure 3b. The calculated surface structures again concur with experimentally observed structures and underline that thermodynamic stability is the driving force in the formation of stable, long-lived terminal surface structures.

However, for this surface, we find that a second terminating structure is predicted to have an identical surface energy to that shown in Figure 8. This second structure (not depicted) exposes a half CAN cage at the crystal surface and has 12 terminal bonds per unit area, just as in the case of the D6R terminated surface. The absence of this termination in the experimental images leads us to speculate that there

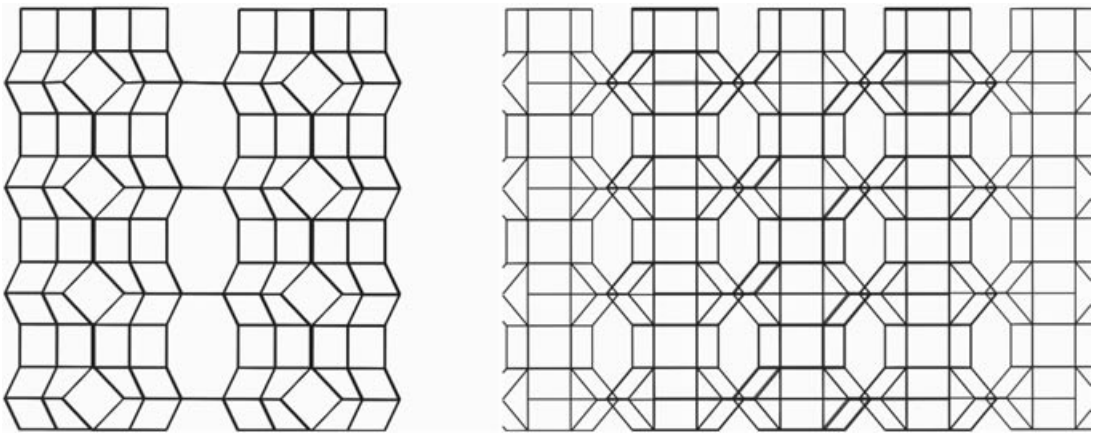

Figure 8. Cross sections of the (001) surface. The left-hand side image is identical to that seen in Figure 3a, whilst the right-hand image is equivalent to the upper part of Figure 3b.

may be a thermodynamic or kinetic component that influences the crystal growth process and results in the preferential exposure of the D6R terminated structure.

Growth along the {001} axis can be considered to arise from two modes of columnar assembly involving CAN and D6R secondary building units. One recognises that columnar assembly may be achieved by fusing CAN cages or by condensation of D6Rs on half-CAN cages. Although the mechanism for columnar assembly is not known, the fact that only the D6R-terminated structure is observed leads us to infer that the half-CAN surface structure, which simulation shows to be thermodynamically stable, may be kinetically unstable with respect to condensation of a D6R. The precise mechanism and intermediate stages of the growth mechanism are currently under investigation using a similar procedure to that used to investigate zeolite Beta C.

Rotational defect: Using interionic potentials developed by Sanders and Catlow,[31] we performed an energy minimisation (molecular dynamics at 0 K) of a $5\times5\times4$ supercell (containing 18000 sites) of purely siliceous LTL using the DL_POLY[32] code. The large number of species that are necessary to describe the rotational defect precluded us from using the GULP software, though the most recent version of GULP contains more efficient Coulomb summation schemes that would, in principle, allow us to compare the results from DL_POLY. Using the relaxed structure, we created the rotational defect consistent with that observed by HREM and again optimised the unit cell contents. The relaxed structure is shown in Figure 9a, whilst Figure 9b shows a magnified region of the defect. It is clear from Figure 9 that the rather large defect actually causes extremely local distortions, which are essentially limited to the first coordination sphere of the oxygen atoms that lie at the boundary between the rotational defect and the remaining perfect crystal. The lattice energy difference between the cell containing the defect and that of the perfect crystal reveals that formation of the defect is favourable by −2.3 eV for the supercell (which corresponds to a ~5 kJ mol^{-1} increase in bond strength for each of the 48 Si−O bonds that join the rotational defect to the unperturbed lattice). The driving force for the formation of the defect arises from short-range bonding forces: the rotation gives rise to a concomitant increase in the T-O-T angle (where T is Si or Al) at the interface between defect and perfect crystal coupled with a reduction in the average bond lengths, as seen in Figure 9b.

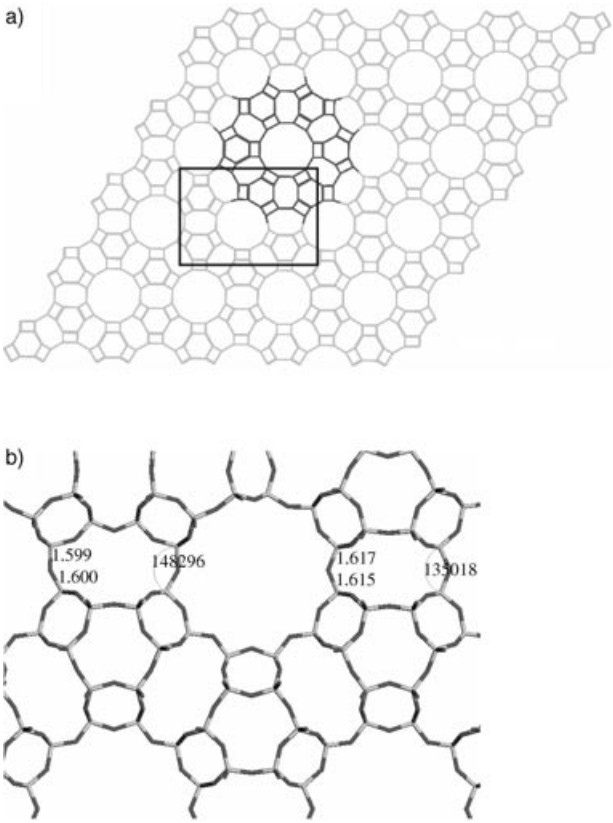

Figure 9. a) The rotational defect is highlighted in bold, and was obtained from optimising the simulation cell; the defect is parallel to the (001) or the *c* crystallographic axis. The highlighted region corresponds b, and shows how the defect is stabilised by forming stronger Si−O bonds at the expense of the optimal Si-O-Si angle.

Analysis of the defect energy shows that although the net change in energy is negative upon formation, the electrostatic or Coulombic component of the energy decreases. The

decrease in attractive electrostatic energy is outweighed by the gain in total lattice energy from strengthening the Si–O bond (associated with a shortening of the bond) and a decrease in the collective interionic repulsive energy. It should be noted that because of the boundary conditions and periodicity of the supercell, the rotational defects are separated by approximately 30 Å. It is therefore conceivable that these defects may be formed at a higher density than has been observed by inspection of the HREM data.

Columnar hole: By using the relaxed supercell described previously, a hole corresponding to the rotational defect (along the {001} axis) was grafted from the crystal and the defective cell contents optimized at constant volume. The resulting structure is depicted in Figure 10 and shows that relaxation around the defect hole is quite minimal.

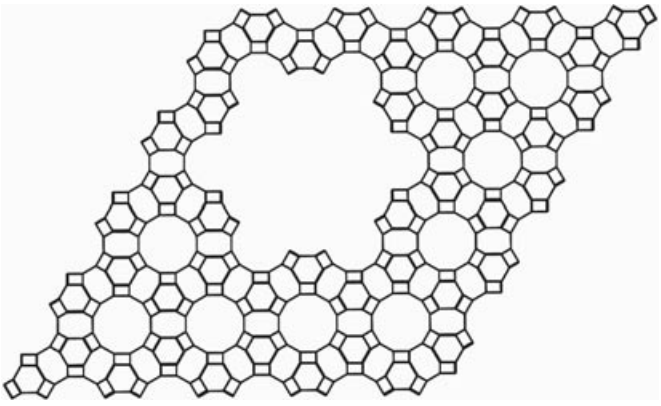

Figure 10. A view down the [001] or crystallographic *c* axis of LTL. The supercell contains a columnar nano-defect.

Although we find that it is energetically unfavourable to create this defect spontaneously in the crystal bulk, we suggest that the defect arises as part of the evolution of crystal growth on contact with the mother liquor or gel. If the defect structure is inspected closely, one realizes that this corresponds to the stepped $\{1\bar{1}0\}$ surface, showing the characteristic single CAN cage termination, and consequently the hole may be perceived as the formation of an additional growth surface, resembling the *external* surface. In porous materials, in which the ratio of internal to external surface area is high, it is perhaps not surprising that nano-voids with structures commensurate with those of the external surface can be formed due to high crystal growth rates. Another possibility is that blockage occurs at the growing surface, preventing registration of SBUs with the growing surface. However, given that the defects extend for the entire length of the crystal and therefore for several hundred angstroms, it is not obvious why the channels are completely empty, as is implied by the electron diffraction along the [001] shown in Figure 6a.

An interesting proposition is that this linear void may arise at the interface between a {110} and $\{1\bar{1}0\}$ overgrowth or even at the interface (grain boundary) between two crystals with {110} and $\{1\bar{1}0\}$ orientations. High growth rates or other kinetic factors may explain why the defect becomes encapsulated within the crystal. However, although the formation of the defect is thermodynamically unfavourable in the perfect bulk structure, the defective zeolitic structure will still have an energy per SiO_2 unit that falls within the ranges which have been identified for a range of zeolitic materials using calorimetric data[33] and theoretical predictions.[34]

These results provide possible explanations of why the columnar defect forms and why very large columnar holes can be observed in both the nanocrystals and single microcrystals. Note that the very large holes show a surface structure that is comparable with a more regular or ideal $\{1\bar{1}0\}$ surface and hence very large holes may be formed where the energetic cost per unit area (i.e. the internal surface energy of the particle) is comparable to the external surface energy.

Discussion

The observations from experimental and simulation evidence suggest that the surface structure of zeolite LTL is extremely well-defined and for the principal growth surfaces, only one structural termination is seen. Comparison of the fine bulk and surface structure evidenced on micro- and nanocrystals reveals the same surface structural motifs, suggesting that the crystal growth mechanism is similar for both materials. The microcrystals have similar morphologies, but their composition is different, one containing pure K, the other a mixture of (principally) Na and K. The nanocrystal is synthesised by using K only, yet its crystal shape is quite different from that of the microcrystal examples. In the nanocrystal, it appears that growth is fastest parallel to the {001} plane and slowest perpendicular to the {001} plane. In the microcrystal, the reverse growth rate appears to be in operation.

Focusing first on the nano and micro pure K LTL syntheses, the Si:Al ratio of the product is approximately 3:1 in both samples; the temperature of synthesis is approximately the same. However, the crystal shapes are different and the molar ratio of Al:K and Si:Al is different in both cases. In the nanocrystal synthesis there is a higher concentration of K and a much higher concentration of Si:Al, compared to those in the microcrystal synthesis. In the nanocrystal synthesis, the duration is six days in comparison to two days in the microcrystal synthesis. In the nanocrystal, growth in the {001} plane is favoured over growth perpendicular to the {001} plane, and in the microcrystal the reverse is seen.

One possible reason for this disparity in growth rates is linked to the probability of reaction and concentration of structural building units in solution. Given the very low concentration of Al in the nanocrystal synthesis reagent mixture, which is required in 25% concentration within the framework, only a very small number of the fragments in solution will contain aluminium. The solution will contain oligomeric siliceous units and a proportion of aluminosilicate units. In the microcrystal synthesis, the proportion of aluminosilicate to purely siliceous units will be much higher. Given that the temperature of synthesis for both materials is

approximately the same, the probability of two solution species being proximate is the same in both cases but the probability that two aluminosilicate fragments undergo a reaction is much lower in the nanocrystal synthesis. The infrequent collision probability will favour growth along the plane that requires the fewest number of bonds to be formed (or events to occur) to polymerise units. In LTL, this will be parallel to the {001} plane or equivalent to growth normal to the $\{1\bar{1}0\}$ plane, since only two bonds are formed on growing this surface, as columns aggregate. In contrast, columnar assembly normal to the {001} plane assembly will be a rare event because six bonds are required to grow the column, and hence the probability of fragments having the correct steric orientation is much lower, therefore growth in this plane is slow. Under the nanocrystal synthesis conditions therefore, flat disc-like morphologies would be predicted from our proposed mechanism, as is observed. At a higher collision probability (in the microcrystal synthesis), two aluminosilicate fragments will have the correct orientation to react far more frequently, hence the thermodynamics or reaction enthalpies of columnar aggregation versus columnar assembly will be very important. On the grounds of thermodynamic stability, cylindrical crystals would be predicted in which the length of the crystal (parallel to [001]) will be greatly in excess of the diameter, because the $\{1\bar{1}0\}$ surface is far more stable than the {001} surface. The crystal formed would expose $\{1\bar{1}0\}$ as the most morphologically important face (with the greatest surface area) and {001} as a less prevalent face (with lower surface area), in accord with the experimentally observed morphology.

If we now turn to a comparison of nano K LTL and micro Na/K LTL, the major point of contrast is that, of course, Na^+ preferentially occupies the extra-framework sites in Na/K LTL and clearly plays an important role in dictating the rate of growth. Crystal growth rates in the [100] and [001] planes are clearly much greater than for the two planes in the nano-synthesis. If a synthesis was performed with the same Si:Al ratio and the same Al:K ratio as used in the nano-synthesis we could infer more about the role of K^+ during the synthesis but this is not the case in the data reported here. In the nanocrystal synthesis, there is a much higher concentration of K^+ in comparison to the microcrystal synthesis. Recently, Gibbs and Lewis[35] reported a atomistic simulation study on low silica zeolite X which showed that the K^+ ion can occupy the D6R and a site immediately above the D6R simultaneously. K^+ ions had been thought to be a key agent to formation of the D6R through empirical observation whilst Na^+ ions are found not to occupy D6R rings. Since the Na^+ ion clearly facilitates much faster growth rates for both crystal planes, it is not clear where the Na^+ ion changes the mode of assembly from fast columnar aggregation/slow columnar assembly to slow columnar aggregation/fast columnar assembly. Because the Si:Al and K ratios and the synthesis duration of the micro K LTL and micro Na/K LTL are different from each other, we cannot single out the role of Na^+ ions. Recent work[36] has shown the delicate relationship between extra-framework cation and aluminium concentration and the crystal growth morphology for columnar MAZ zeolites. It would therefore be interesting to attempt a similar systematic synthesis approach to the LTL system to explore how minute variations in the reagents affect the product. Another experiment of interest would be to extend the synthesis duration of the nanocrystal synthesis to observe whether the growth rate of either or both of the planes changes as a function of length scale. It is possible that the diffusion-limited growth may become important at a critical crystal size, though our work,[37] and that of Agger and co-workers[38] strongly suggests that zeolite growth is surface-controlled.

To try and probe the growth mechanism in more detail, we focused on the nature of the principal growth unit. We began by addressing the nature of the crystal growth mechanism on the {001} plane, where columnar assembly is crucial. The observation of a D6R terminated surface structure, with no evidence of a structure where the D6R is absent (as is the case in Faujasite[39]) suggests that the D6R is part of a larger growth unit, or that the condensation of a D6R onto the crystal surface is so rapid (perhaps both thermodynamically and kinetically unstable with respect to formation of the D6R surface) that a surface denuded of a D6R is never observed. What is unclear from our observations is the identity of the solution species, however, Serre et al.[40] and others including Knight (see[41] for example) and Engelhardt (see[42] for example), have demonstrated the utility of NMR methods in identifying solution species, and we expect to utilize this invaluable technology in future work. Notwithstanding existing experimental evidence, a possible building unit for the {001} surface is proposed in Figure 11, which can

Figure 11. A possible secondary structural building unit that may dictate columnar growth in zeolite L.

be regarded as a double 6-ring, capped by 4-rings or a 'half'-CAN unit, capped with a 6MR. Repeated condensation of these units with one another generates the familiar columnar structure, provided the D6R reacts with the open half-CAN structure of another unit. Each columnar structure can then aggregate to generate the familiar 12 MR decorated by six columns. The evidence that the SBU proposed is the key building unit is phenomenological and so to provide a more rigorous insight into thermodynamics of growth in a forthcoming paper,[20] we will describe a first-principles study of which fragments are most stable in solution and how these fragments combine to define a mechanism of columnar assembly.

On the topic of rotational defects, although formation of the rotational defect is energetically favourable, we believe that the low concentration of these defects in actual samples suggests that there is a substantial barrier that prevents their spontaneous formation in the bulk crystal. The rotation in bulk would involve breaking partially covalent bonds and is

therefore extremely unlikely to occur at moderate temperatures. For this reason, we speculate that the defect is grown in at the surface, where the misalignment of a CAN (or some other) growth unit with the surface is more facile because a small number of bonds could anchor the SBU on the surface in a misaligned configuration. The 12-ring surrounded by six CAN/D6R columns can be likened to a nano-wheel. In the perfect crystal, each wheel is in perfect tessellation with wheels in the same plane. In the defective material, although the structure of the wheel is *identical*, the wheels no longer have a periodic repeat length and no longer tessellate. Once one CAN misaligns with the surface, this could nucleate the rotational defect. Within the rotational defect, the rotation of one of the six columns containing D6R/CAN is calculated to be extremely energetically unfavourable. Therefore, when one CAN condenses upon the surface, misaligned by 30°, addition of the remaining five columns occurs, generating the core structure that is identical to that in the perfect material. The fact that the defects can be observed in close proximity to the surface in Figure 4 lends credence to the proposition that the defect is born at the surface.

The observation of columnar holes cannot currently be explained unequivocally. We have presented a number of possible explanations for their existence but we are unable at this stage to categorically state their origin. That these defects are obtained in both nano- and microcrystals suggests that their appearance may not be driven by kinetic factors.

We return finally to the observation of stacking faults in LTL and the reconstruction or coincidence boundary reported by Terasaki,[22] where the fault lies parallel to the {001} plane. One explanation of this phenomenon is that the probability of a SBU attaching upon the surface at a non-ideal lattice site, overlapping an interstice for example, increases considerably as the temperature and growth rates increase. The {001} plane exposes a high density of silanol groups per unit area, much more so than on the $\{1\bar{1}0\}$ plane. The sticking probability of an SBU to the {001} surface will be much higher than on the $\{1\bar{1}0\}$ plane. We believe the corrugated nature of the surface that exposes silanol groups in high concentrations, will facilitate relatively unfavourable registrations of SBUs upon the surface. Although, it is less thermodynamically favourable to introduce the coincidence boundary into the crystal than to perpetuate the perfect crystal, the kinetics dictate that statistically a relatively unfavourable condensation will be attempted. Provided the barrier to condensation is small enough, and the barrier to dissolution large enough, such an event could occur and thus nucleate the coincidence boundary. An inference one could make from this assertion is that to prepare non-faulted crystals for optimal crystallinity, the temperature of the synthesis should be kept as low as possible. Empirically, it is found that lower temperatures promote defect-free crystals.

In conclusion, atomic scale resolution of perfect and defective microporous LTL coupled with atomistic simulation have provided new insights into the thermodynamic and kinetic factors that influence crystal growth of zeolites and the crystal habit. We consider that a combination of methods affords a powerful and systematic means of investigating the growth of perfect and faulted microporous materials.

Acknowledgement

B.S. and O.T. thank Sir John Meurig Thomas for his continued support and for his valuable comments on this manuscript.

[1] D. W. Breck, N. A. Acara, US Patent 3,216,789, **1965**.
[2] R. M. Barrer, H. Villiger, *Z. Kristallogr.* **1969**, *128*, 352.
[3] G. Artioli, A. Kvick, *Eur. J. Mineral.* **1990**, *2*, 749.
[4] J. R. Bernard, US Patent 4,104,320, **1978**.
[5] J. R. Bernard, *5th International Zeolite Conference*, *Vol. 689*, Hayden Press, (London), **1980**.
[6] T. R. Hughes, W. C. Buss, P. W. Tamm, R. L. Jacobson, *Proceedings of the 7th International Zeolite Conference*, *Vol. 725*, Elsevier/IZA, Amsterdam, **1987**.
[7] S. J. Tauster, J. J. Steger, *Mater. Res. Soc. Symp. Proc. Vol. 111*, **1987**, p. 419.
[8] O. Terasaki, K. Yamazaki, J. M. Thomas, T. Ohsuna, D. Watanabe, J. V. Sanders, J. C. Barry, *Nature* **1987**, *330*, 58.
[9] G. Calzaferri, M. Pauchard, H. Maas, S. Huber, A. Khatyr, T. Schaafsma, *J. Mater. Chem.* **2002**, *12*, 1.
[10] M. M. J. Treacy, *Microporous Mesoporous Mater.* **1999**, *28*, 271.
[11] R. M. Barrer, C. Baerlocher, *Z. Kristallogr.* **1972**, 136.
[12] D. E. W. Vaughan, US Patent 4,552,731, **1985**.
[13] D. E. W. Vaughan, US Patent 4,554,146, **1985**.
[14] T. Wortel, US Patent 4,544,539, **1985**.
[15] R. M. Barrer, D. E. Mainwaring, *J. Chem. Soc. Dalton Trans.* **1972**, 1259.
[16] D. E. W. Vaughan in *Zeolite Catalysis for the Solution of Environmental Problems*, (Ed. K. G. Ione), Nova. Sci., New York, **1995**, p. 423.
[17] D. E. W. Vaughan, *Stud. Surf. Sci. Catal. Vol 65*, Elsevier, Amsterdam, **1991**, 275.
[18] O. Terasaki, T. Ohsuna, V. Alfredsson, J. O. Bovin, D. Watanabe, S. W. Carr, M. W. Anderson, *Chem. Mater.* **1993**, *5*, 452.
[19] B. Slater, C. Richard, A. Catlow, Z. Liu, T. Ohsuna, O. Terasaki, M. A. Camblor, *Angew. Chem.* **2002**, *114*, 1283; *Angew. Chem. Int. Ed.* **2002**, *41*, 1235.
[20] B. Slater, J. D. Gale, C. R. A. Catlow, T. Ohsuna, O. Terasaki, unpublished results.
[21] I. S. Kerr, J. A. Gard, R. M. Barrer, I. M. Galabova, *American Mineralogist* **1970**, 55.
[22] O. Terasaki, J. M. Thomas, S. Ramdas, *J. Chem. Soc. Chem. Commun.* **1984**, 216.
[23] J. M. Thomas, O. Terasaki, P. L. Gai, W. Z. Zhou, J. Gonzalez-Calbet, *Acc. Chem. Res.* **2001**, *34*, 583.
[24] X. Meng, Y. Zhang, C. Meng, W. Pang, Proceedings of the 9th International Zeolite Conference (Ed.: R. von Ballmoos), Butterworth-Heinemann, **1993**.
[25] S. L. Qui, Jilin University, **2001**.
[26] T. Ohsuna, Y. Horikawa, K. Hiraga, O. Terasaki, *Chem. Mater.* **1998**, *10*, 688.
[27] B. Slater, J. O. Titiloye, F. M. Higgins, S. C. Parker, *Curr. Opin. Solid State Mater. Sci.* **2001**, *5*, 417.
[28] D. H. Gay, A. L. Rohl, *J. Chem. Soc. Faraday Trans.* **1995**, *91*, 925.
[29] L. Whitmore, B. Slater, C. R. A. Catlow, *Phys. Chem. Chem. Phys.* **2000**, *2*, 5354.
[30] J. D. Gale, A. L. Rohl, *Mol. Simul.* **2003**, *29*, 291.
[31] M. J. Sanders, M. Leslie, C. R. A. Catlow, *J. Chem. Soc. Chem. Commun.* **1984**, 1271.
[32] W. Smith, C. W. Yong, P. M. Rodger, *Mol. Simul.* **2002**, *28*, 385.
[33] I. Petrovic, A. Navrotsky, M. E. Davis, S. I. Zones, *Chem. Mater.* **1993**, *5*, 1805.
[34] N. J. Henson, A. K. Cheetham, J. D. Gale, *Chem. Mater.* **1994**, *6*, 1647.
[35] T. Gibbs, D. W. Lewis, *Chem. Commun.* **2002**, 2660.

[36] A. M. Goossens, E. J. P. Feijen, G. Verhoeven, B. H. Wouters, P. J. Grobet, P. A. Jacobs, J. A. Martens, *Microporous Mesoporous Mater.* **2000**, *35–36*, 555.
[37] M. Mistry, B. Slater, C. R. A. Catlow, unpublished results.
[38] J. R. Agger, N. Hanif, C. S. Cundy, A. P. Wade, S. Dennison, P. A. Rawlinson, M. W. Anderson, *J. Am. Chem. Soc.* **2003**, *125*, 830.
[39] V. Alfredsson, T. Ohsuna, O. Terasaki, J. O. Bovin, *Angew. Chem.* **1993**, *105*, 1262; *Angew. Chem. Int. Ed. Engl.* **1993**, *32*, 1210.
[40] C. Serre, F. Taulelle, G. Fereya, *Chem. Commun.* **2003**, 2755.
[41] C. T. G. Knight, R. T. Syvitski, S. D. Kinrade, in *Zeolites: A Refined Tool for Designing Catalytic Sites*, *Vol. 97*, **1995**, p. 483.
[42] G. Engelhardt, D. Hoebbel, *J. Chem. Soc. Chem. Commun.* **1984**, 514.

Received: December 23, 2003
Revised: May 7, 2004
Published online: August 27, 2004

